

Wave Propagation and Absorption in ECR Plasma Thrusters

IEPC-2017-105

*Presented at the 35th International Electric Propulsion Conference
Georgia Institute of Technology – Atlanta, Georgia – USA
October 8–12, 2017*

Mario Merino^{*}, Álvaro Sánchez-Villar[†], Eduardo Ahedo[‡]
Equipo de Propulsión Espacial y Plasmas (EP2), Universidad Carlos III de Madrid, Leganés, Spain

Paul Bonoli, Jungpyo Lee, Abhay Ram and John Wright
Plasma Science and Fusion Center, Massachusetts Institute of Technology, MA, USA

The physical mechanisms involved in the generation, propagation and absorption of microwaves in electron-cyclotron-resonance plasma thrusters, and their relevance in the operation of these devices, are discussed. The features of the electromagnetic waves and electron motion near the resonance region are analyzed with a one-dimensional model. The characteristics of the two-dimensional wave-plasma problem are examined, and a trade-off of different numerical models is presented as a first step toward the development of an ECR wave-plasma interaction simulation code.

I. Introduction

Electron Cyclotron Resonance (ECR) has been successfully used to generate and heat up plasmas since the 1960's. In 1960, the energization of a magnetoplasma with microwave power by electron cyclotron resonance heating (ECRH) was first observed experimentally in the Oak Ridge energetic-ion trapping program. Afterwards, theoretical and experimental efforts were made to obtain a consistent unified theory of ECR phenomena. Amongst the main applications of ECR phenomenology, noteworthy are ECR emission and absorption for fusion plasmas[1] and the design of ECR ion sources (ECRIS)[2]. ECRIS have been found to be a useful technology for various applications such as atomic physics and plasma etching[3]. The combination of an ECR source with a magnetic nozzle (MN) has also been proposed as a plasma thruster for space propulsion[4–9]. In this concept, microwaves of a few GHz are used to generate and energize a plasma that then expands in a divergent magnetic field to generate thrust contactlessly.

As could be expected, the plasma-wave interaction problem is central to ECR thrusters and any other ECR applications. The complexity of this problem is high, as it results from the interplay of multiple simultaneous phenomena, including wave propagation, absorption, cutoffs, reflections, resonances and mode conversions[10–13]. All these mechanisms depend on the plasma and magnetic parameters, in particular the plasma density and collisionality, the magnetic field strength and direction, and the geometry and boundary conditions of the domain. Moreover, to a large extent, especially near resonances, propagation and absorption are affected by plasma temperature, kinetic features, inhomogeneities, and bulk plasma velocity. Lastly, while the abovementioned phenomena are linear, non-linear interactions also exist in the case of high-amplitude waves. In order for an ECR source to operate successfully and heat the plasma, the wave must be able to propagate through the plasma and reach the resonance regions where it is absorbed without being reflected, a problem known as accessibility[14].

Substantial effort has been dedicated to understand and model the mechanisms that govern the propagation and absorption of electromagnetic waves in a plasma near the ECR [15–19]. On the one hand, ray

^{*}Assistant Professor, Aerospace Engineering department, mario.merino@uc3m.es.

[†]PhD student, Aerospace Engineering department.

[‡]Professor, Aerospace Engineering department.

and beam tracing algorithms [20–22] have been successfully employed to analyze the propagation and accessibility problems. These methods rely either on a cold plasma or on a kinetic dielectric tensor description, and work remarkably well in regions where the WKB condition is satisfied, i.e., wherever the wavelength is much smaller than the characteristic gradient lengths in the plasma or magnetic field. This, unfortunately, excludes the neighborhood of resonances and cutoffs. Given their small size, often comparable to the wavelength, ray and beam tracing schemes are not the best approach to model ECR thrusters. On the other hand, full-wave models attempt to solve Maxwells equations directly in the simulation domain, either in the time[23, 24] or frequency domain[25–27], and either in 1D, 2D or 3D geometries.

In spite of these experimental and modeling efforts and the plethora of existing techniques, the understanding of the plasma-wave problem in ECR thrusters is still far from complete, and at present, a predictive model that can explain power deposition and be used to optimize the thruster design is still lacking. The H2020 project MINOTOR[28] aims to demonstrate the feasibility of the ECR thruster technology as a disruptive game-changer in electric propulsion, with an in-depth numerical and experimental investigation plan to bring the technology from TRL3 to TRL5. A core part of this project is to improve the present understanding of the plasma-wave interaction problem and develop a complete ECR thruster simulation code, including the propagation and deposition of electromagnetic power in the plasma.

This paper presents a preliminary study on the modeling of the plasma-wave interaction problem of ECR thrusters carried out in the frame of the MINOTOR project, defines the code to be developed, and describes the planned next steps. The objectives of this paper are twofold. First, it aims to provide a unified review of several fundamental physical mechanisms and phenomena involved in the wave problem of ECR thrusters and their relevance in its operation. Second, it compares and discusses the available full-wave numerical approaches to integrate the problem and studies their issues and limitations.

The rest of the paper is structured as follows. Section II overviews in more detail ECR plasma thrusters. Section III reviews the propagation and absorption of waves in a one dimensional plasma, summarizing the main dependencies with plasma and magnetic field parameters. Section IV discusses different alternatives for two- (and three-)dimensional full-wave numerical modeling, comparing their advantages and disadvantages. The numerical dispersion, diffusion, dissipation, and the existence of spurious solutions, are commented upon for various solution schemes.

Finally, Section V gathers conclusions and outlines the planned next steps in this work.

II. ECR plasma thrusters

The ECR thruster belongs to the family of *electrodeless plasma thrusters* together with the Helicon Plasma Thruster (HPT)[29–32], a new generation of electric thrusters that promises improvements the classical gridded ion engines and Hall effect thrusters [33]. The absence of electrodes eliminates the associated erosion issues, opening the possibility of much larger thruster lifetimes than existing technologies. The acceleration of a quasineutral plasma jet means that no neutralizer is required. This results in a simple thruster and PPU design, and the possibility of using many propellant types. It is expected that these thrusters will yield high thrust densities, scale easily from mid-low to high powers, and allow an ample throttleability.

An ECR thruster consists of an ionization chamber, a set of solenoids or permanent magnets that set up a magnetic field, a propellant injector, and a radiating element, which can be a microwave antenna or a waveguide. An example configuration is sketched in Fig. 1. The device can be roughly decomposed into an internal domain, where electromagnetic power ionizes the propellant gas and heats up the resulting plasma, and an external domain or magnetic nozzle, where the applied magnetic field channels the acceleration of the plasma, generating magnetic thrust contactlessly. Optionally, the magnetic nozzle can be used to steer laterally the plasma jet, thus obtaining a form of thrust vector control that does not rely on moving parts[34]. Besides creating the external magnetic nozzle, the applied magnetic field has two other key roles in the operation of the device. First, it enables the electromagnetic waves to propagate in the plasma and creates the resonance conditions at specific locations of the internal domain. Second, it decreases the plasma transport toward the walls, reducing efficiency losses and mitigating their heating and erosion.

The inception of ECR plasma thrusters took place in the 1960’s, when a few prototypes were built and tested using different wave sources, injection profiles, etc[4, 5]. Results showed over 95% of the incident power deposited in the plasma. Reportedly, based on preliminary thrust measurements, thrust efficiencies of up to 40% with about 3200 s of I_{sp} at 912 W of power could be attainable[4]. Noteworthy is the work of Sercel et al.[6–8], who also developed a few-kW thruster prototype. Besides advancing the modeling of the

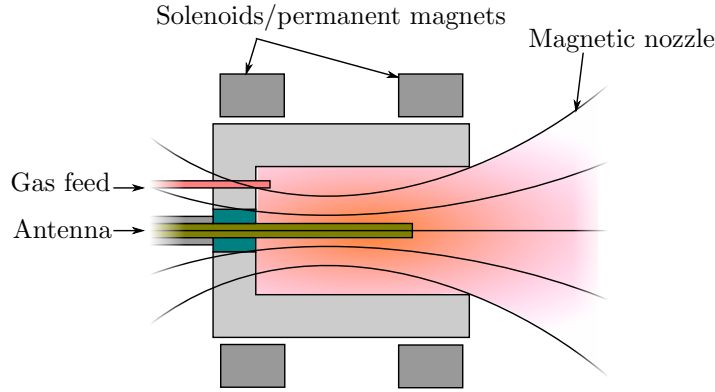


Figure 1. Sketch of an ECR thruster that represents the current ONERA prototype. Gas, usually xenon or argon, is fed into the thruster chamber by means of a gas feed. Injection can be done radially/azimuthally too. Solenoids or permanent magnets are used to generate the desired magnetic field topology inside the thruster, and the magnetic nozzle outside of it. A central dipole antenna radiates microwave power at a frequency that matches the ECR resonance in a certain region of the magnetic field, heating up electrons and ionizing the gas into a plasma. Alternatively, a waveguide can be used. The resulting hot plasma expands in the external magnetic nozzle to generate magnetic thrust contactlessly.

plasma generation and transport in the device, they attributed the power losses to plasma diffusion toward the walls, and argued that radiative losses are less than previously estimated by other groups. The interest on ECR thrusters resurfaced in the last decade with the work at ONERA[9]. A small-size low-power device (< 100 W) was developed and tested successfully, reportedly reaching high thrust efficiencies for a device in this power range ($\sim 16\%$). Although previous experiments used transverse-electric (TE) modes and axial waveguides[4–6], ONERA' prototype uses a central antenna to launch the microwaves. A summary table of the main design and performance parameters of these three devices is shown in Table 1.

	Miller[4, 5]	Sercel[6–8]	ONERA[9]
Diameter [mm]	51	128	13 – 27
Length [mm]	51	~ 50	15
Propellant species	Xe/Ar	Ar	Xe/Ar
Power range [W]	$10^3 - 10^4$	$10^2 - 10^4$	10^2
Frequency [GHz]	8.35	2.12	2.45
Applied field B_0 [G]	2983	755	875
Axial field gradient α [m^{-1}]	~ 6.5	~ 2	~ 0.07
Electron temperature T_e [eV]	10^2	35	10 – 30

Table 1. Illustrative parameter values of the existing ECR thruster, based on or estimated from the references given.

III. One-dimensional wave propagation and absorption

The propagation of electromagnetic waves is governed by Maxwell equations, i.e.,

$$\nabla \times \mathbf{E} = -\frac{\partial \mathbf{B}}{\partial t}; \quad (1)$$

$$\nabla \times \mathbf{B} = \mu_0 \varepsilon_0 \frac{\partial \mathbf{E}}{\partial t} + \mu_0 (\mathbf{j}_p + \mathbf{j}_a); \quad (2)$$

$$\nabla \cdot \mathbf{E} = (\rho_p + \rho_a)/\varepsilon_0; \quad (3)$$

$$\nabla \cdot \mathbf{B} = 0, \quad (4)$$

where \mathbf{j}_p, ρ_p represent the plasma electric current density and charge density that result from the all charged species, and \mathbf{j}_a, ρ_a are generic forcing terms used to describe the electric current density and charge density in the antenna of the device, if any.

Equations (1) to (4) must be solved together with the kinetic equations of each plasma species to close the model. The general problem is nonlinear, and the plasma current and charge \mathbf{j}_p, ρ_p depend on the value of the electromagnetic fields and the distribution function of each species in the past light cone[10, 35].

Due to the complexity of this approach, several approximation of varying level of sophistication are used. In the standard kinetic tensor description of the plasma, the kinetic equations are linearized and the plasma is assumed to be infinite and uniform. Then, Fourier/Laplace analysis in time and space allows expressing the plasma contribution \mathbf{j}_p, ρ_p through a dielectric tensor form $\boldsymbol{\kappa}$, which is a function of the frequency and the wave number[10]. Plasma inhomogeneities and boundaries limit the validity of this solution[36]. A further simplification of the model ignores the thermal dispersion of the plasma species and treats it as cold. Then, the spatial dependency of \mathbf{j}_p, ρ_p becomes *local*, so the tensor $\boldsymbol{\kappa}$ is no longer a function of the wave number. The cold plasma approximation is only valid as long as the wave phase velocity is larger than the electron thermal velocity. The cold plasma tensor theory retains the relevant physics to study many of the plasma-wave interaction problems, including propagation, cutoffs, and accessibility. It also allows identifying the fundamental resonances. Other aspects, such as resolving those resonances, mode conversions, and harmonic resonances can be addressed with a kinetic plasma tensor formulation. Nonetheless, only the full Maxwell-Vlasov formulation is strictly self-consistent in finite or inhomogeneous plasmas, or when nonlinear effects are important.

Combining Eqs. (1) and (2) allows eliminating the wave magnetic field \mathbf{B} . From a cold plasma perspective, we can then write the following expression in the frequency domain:

$$\nabla \times (\nabla \times \hat{\mathbf{E}}) = -\nabla^2 \hat{\mathbf{E}} + \nabla (\nabla \cdot \hat{\mathbf{E}}) = \frac{\omega^2}{c^2} \boldsymbol{\kappa} \cdot \hat{\mathbf{E}} + i\omega\mu_0 \hat{\mathbf{j}}_a, \quad (5)$$

where $\mathbf{E} = \Re[\hat{\mathbf{E}} \exp(-i\omega t)]$. We can further expand the fields also in the wave number domain, writing $\mathbf{E} = \Re[\tilde{\mathbf{E}} \exp(i\mathbf{k} \cdot \mathbf{r} - i\omega t)]$, where $\mathbf{k} \in \mathbb{C}^3$ is the complex wavenumber. Then, Eq. (5) can be rearranged as

$$\left[\begin{pmatrix} -k_y^2 - k_z^2 & k_x k_y & k_x k_z \\ k_x k_y & -k_x^2 - k_z^2 & k_y k_z \\ k_x k_z & k_y k_z & -k_x^2 - k_y^2 \end{pmatrix} + \frac{\omega^2}{c^2} \begin{pmatrix} \kappa_{xx} & \kappa_{xy} & \kappa_{xz} \\ \kappa_{yx} & \kappa_{yy} & \kappa_{yz} \\ \kappa_{zx} & \kappa_{zy} & \kappa_{zz} \end{pmatrix} \right] \cdot \begin{bmatrix} \tilde{E}_x \\ \tilde{E}_y \\ \tilde{E}_z \end{bmatrix} = -i\omega\mu_0 \begin{bmatrix} \tilde{j}_{ax} \\ \tilde{j}_{ay} \\ \tilde{j}_{az} \end{bmatrix}. \quad (6)$$

The nontrivial solutions of the homogeneous version of this equation are the roots of the determinant of the matrix that multiplies \mathbf{E} ; this is known as the wave *dispersion relation*.

If the local z axis is chosen in the direction of the applied magnetic field \mathbf{B}_0 , a non-unitary, orthogonal complex vector basis $B : \{\mathbf{e}_+, \mathbf{e}_-, \mathbf{e}_z\}$ can be defined as

$$\mathbf{e}_+ = \begin{bmatrix} 1 \\ -i \\ 0 \end{bmatrix}, \mathbf{e}_- = \begin{bmatrix} 1 \\ i \\ 0 \end{bmatrix}, \mathbf{e}_z = \begin{bmatrix} 0 \\ 0 \\ 1 \end{bmatrix}. \quad (7)$$

The \mathbf{e}_+ and \mathbf{e}_- components for the electric field $\hat{\mathbf{E}}$ and $\hat{\mathbf{v}}$ in this basis are given by

$$\hat{E}_\pm = \frac{1}{2} (\hat{E}_x \pm i\hat{E}_y), \quad \hat{v}_\pm = \frac{1}{2} (\hat{v}_x \pm i\hat{v}_y) \quad (8)$$

and the cold plasma dielectric tensor $\boldsymbol{\kappa}$ in this basis is diagonal:

$$\boldsymbol{\kappa} = \begin{bmatrix} L & 0 & 0 \\ 0 & R & 0 \\ 0 & 0 & P \end{bmatrix}, \quad (9)$$

where[10]:

$$L = 1 - \sum_s \frac{\omega_{ps}^2}{\omega(\omega + i\nu_e - \omega_{cs})}, \quad R = 1 - \sum_s \frac{\omega_{ps}^2}{\omega(\omega + i\nu_e + \omega_{cs})}, \quad P = 1 - \sum_s \frac{\omega_{ps}^2}{\omega(\omega + i\nu_e)}. \quad (10)$$

Parameters ω_{ps} and ω_{cs} are respectively the plasma frequency and gyrofrequency of species s . For electrons, in particular:

$$\omega_{pe}^2 = \frac{e^2 n_0}{\epsilon_0 m_e}, \quad \text{and} \quad \omega_{ce} = \frac{eB}{m_e}. \quad (11)$$

The L , R and P stand for left-hand, right-hand and plasma terms, as they define the dispersion relation of the right-hand and left-hand circularly polarized waves and plasma oscillations. At microwave frequencies, the ion contribution to κ is small and can be neglected in first approximation.

A. Parallel wave propagation

When the propagation direction is parallel to the magnetic field, $\mathbf{k} = k\mathbf{e}_z$, the wave equations for \hat{E}_+ , \hat{E}_- and \hat{E}_z are fully uncoupled. The \hat{E}_- field, in particular, describes the right-hand side polarized wave (RHP). It is known that the main mechanism for the absorption of energy in ECR discharges[13] is the resonance of the RHP waves when $\omega = \omega_{ce}$. In order to study the propagation and absorption of RHP waves one can study the solutions of the parallel one-dimensional RHP wave equation. Neglecting the contribution of the ions to the dielectric tensor, it can be expressed as:

$$\frac{d^2 \hat{E}_-}{dz^2} + \underbrace{\frac{\omega^2}{c^2} \left(1 - \frac{\omega_{pe}^2(z)}{\omega [\omega - \omega_{ce}(z) + i\nu_e(z)]} \right)}_{n^2} \hat{E}_- = 0, \quad (12)$$

where n^2 is the squared refractive index. Following a similar approach to Refs. 13, 17, equation (12) is expressed in non-dimensional form. Assumptions are made that ω_{pe}, ν_e are independent of z and that around the resonance point the magnetic field can be expanded as:

$$\omega_{ce}(z) = \omega(1 + \alpha z) \quad \text{being} \quad \alpha = \left| \frac{1}{B_0} \left(\frac{dB}{dz} \right)_{z=0} \right|. \quad (13)$$

As a result equation (12) reduces to:

$$\frac{d^2 \hat{E}_-}{ds^2} + \left(1 + \frac{\eta}{s - i\gamma} \right) \hat{E}_- = 0, \quad (14)$$

where

$$\eta = \frac{\omega_{pe}^2}{\omega c \alpha}, \quad \gamma = \frac{\nu_e}{c \alpha}, \quad \text{and} \quad s = \frac{\omega}{c} z. \quad (15)$$

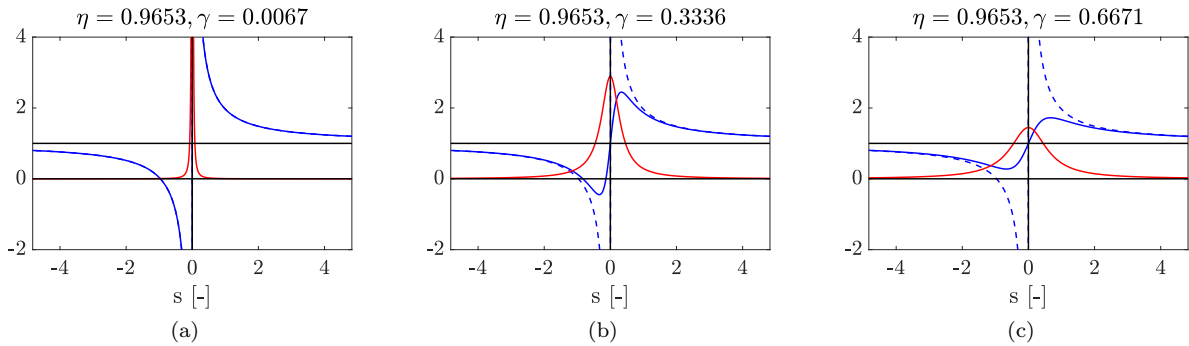


Figure 2. Square of the refractive index along a channel where B_0 decreases linearly, for $\eta \approx 0.9653$ and (a) $\gamma \approx 0.0267$ (b) $\gamma \approx 0.3336$ (c) $\gamma \approx 0.6004$. In blue and red, the real and imaginary parts of the refractive index squared. The dashed line shows the real part in the collisionless limit for reference.

The refractive index has a pole at $s = i\gamma$ and a zero at $s = -\eta + i\gamma$, representing a resonance and a cutoff accordingly as shown in Fig. 2(a). These points are also called a *singular turning point* and a *linear turning point*. The region between both is defined as the *evanescent region* where the refractive index has a large imaginary component.

Budden [37] explored the solutions to Eq. (14), which is also the non-dimensional form for radio waves propagating in the ionosphere. Asymptotic expressions and series expansion on Whittaker functions, members of the confluent hypergeometric functions family[38], were found. Using these results, Budden found relations for the transmission and reflection coefficients when the incident wave approached the cutoff-resonance system from the cutoff side or from the resonance side, making remarks on the absorption as well. The asymptotic value of the RHP electric field in these two cases is given next, and a summary of the transmission and reflection coefficients is shown in Table 2.

CASE I. APPROACHING THE RESONANCE-CUTOFF FROM THE CUTOFF SIDE.

$$s \rightarrow \infty : \hat{E}_- = \exp(-\pi\eta/2) \exp(is + \eta \ln|2s|/2) \quad (16)$$

$$s \rightarrow -\infty : \hat{E}_- = \exp(is + i\eta \ln|2s|/2) - \frac{2\pi i \exp(-\pi\eta/2)}{(-i\eta/2)!(-1 - i\eta/2)!} \exp(-is - i\eta \ln|2s|/2) \quad (17)$$

The last expression includes an incident and a reflected wave.

CASE II. APPROACHING THE RESONANCE-CUTOFF FROM THE RESONANCE SIDE.

$$s \rightarrow \infty : \hat{E}_- = \exp(-is - \eta \ln|2s|/2) \quad (18)$$

$$s \rightarrow -\infty : \hat{E}_- = \exp(-\pi\eta/2) \exp(is + \eta \ln|2s|/2) \quad (19)$$

Note that Eqs. (17)–(18) have been adapted to our sign convention and nomenclature. The solution to Eq. (12) for a single wave can also be approximated with a WKB expansion whenever the refractive index changes smoothly and thus the gradients are small. In practice, this means away from the cutoff-resonance region.

$$\hat{E}_-(z) = n^{-1/2}(z) \hat{E}_{r0} \exp\left(\pm i \frac{\omega}{c} \int^z n(z') dz'\right), \quad \text{valid when } \frac{c^2}{\omega^2} \left| \frac{3}{4} \left(\frac{1}{n^2} \frac{dn}{dz} \right)^2 - \frac{1}{2n^3} \frac{d^2n}{dz^2} \right| \ll 1. \quad (20)$$

	CASE I	CASE II
$ R $	$1 - e^{-\pi\eta}$	0
$ T $	$e^{-\pi\eta/2}$	$e^{-\pi\eta/2}$
$ R ^2 + T ^2$	$1 - e^{-\pi\eta} + e^{-2\pi\eta} < 1$	$e^{-\pi\eta} < 1$

Table 2. Summary of transmission and reflection coefficients[10]. The last line of the table indicates that the sum of reflected and transmitted power is less than the incident power. The missing power is absorbed at the resonance.

The full numerical solution of Eq. (14), using Eqs. (16) and (19) and their derivatives to set up the boundary conditions for integration, is shown in Figs. 3 and 4 in the two cases. The range of parameters used amply covers the range of operation regimes of in Table 1.

Parameter η controls the length of the evanescent region. If this length is relatively small with respect to the wavelength, i.e., if $\eta \ll 1$, the incident wave tunnels through the evanescent region. However, when $\eta \sim 1$, tunneling is negligible, and the absorption and reflection is dominated by the first turning point found by the wave (i.e., the cutoff or the resonance, depending the direction of propagation). Note that independently of the case, there is a net absorption. It can be noticed that the numerical solution approaches the asymptotic solution in all cases for $|s| \gg \eta$.

The refractive index is infinite at $s = 0$ in the collisionless limit, as shown in Fig. 2. The inclusion of an effective collisionality ν_e , described by the parameter γ , displaces the pole to the imaginary axis and limits the value of n reached at the resonance. Moreover, as can be observed in that figure, the evanescent region is shortened as γ increases. A second cutoff between $s = \eta/2$ and $s = 0$ appears, that converges with the first as γ increases. For $\gamma \geq \eta/2$, the real part of the refractive index squared is never negative in the domain. Nevertheless, the strong refractive index gradients in this region still produce some reflection in case I. Even if the maximum value of the imaginary part of the refractive index decreases as γ increases, the thickness of the region where damping is important around the resonance grows.

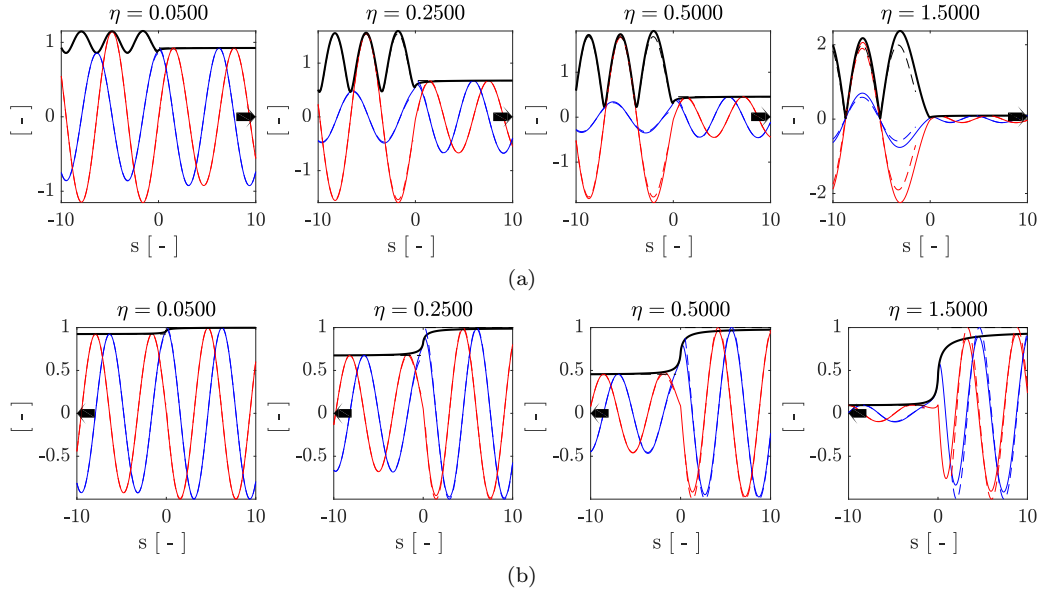


Figure 3. Effect of the dimensionless parameter η on the wave propagation through resonance, for $\gamma = 0.0067$. Blue and red lines refer to real and imaginary parts of the complex amplitude of the RHP electric field \hat{E}_- . The black line shows the magnitude of \hat{E}_- . Solid and dashed lines refer to numerical and analytic solutions. The upper plots correspond to Case I, the lower plots to Case II.

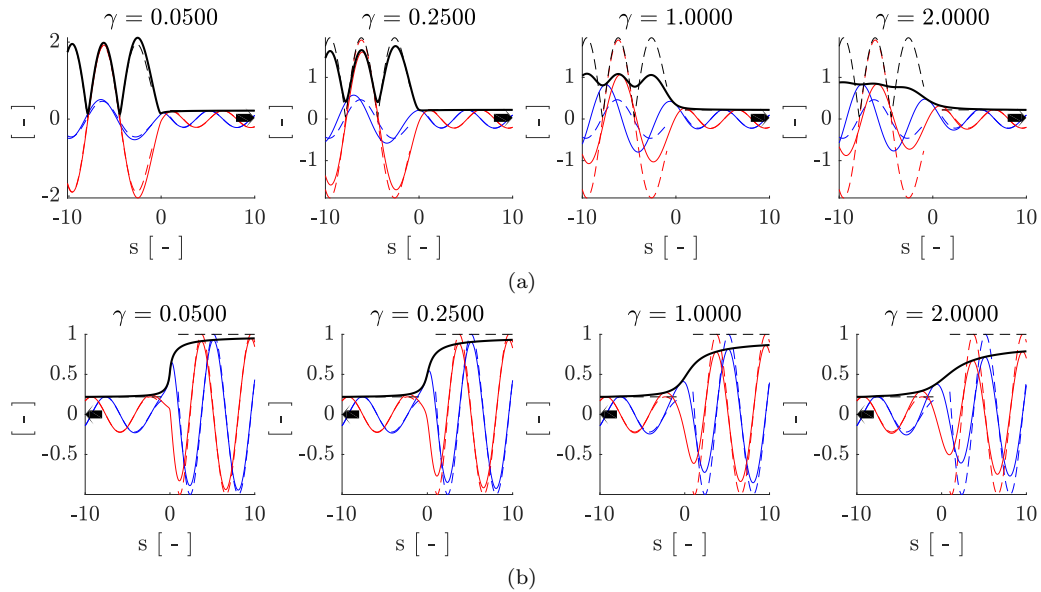


Figure 4. Effect of the dimensionless parameter γ on the wave propagation through resonance, for $\eta = 0.9653$. Blue and red lines refer to real and imaginary parts of the complex amplitude of the RHP electric field \hat{E}_- . The black line shows the magnitude of \hat{E}_- . Solid and dashed lines refer to numerical and analytic solutions. The upper plots correspond to Case I, the lower plots to Case II.

The ratios of reflected, transmitted and absorbed power are however independent of γ in first approximation. In both cases I and II, transmission has the same dependence on η . Reflection, on the other hand, only takes place in case I. This means that Case I has a maximum in the absorbed power that can be found analytically at $\eta = \eta^* = \ln 2/\pi \approx 0.2206$ for which the absorption is estimated to be $1 - |R|^2 - |T|^2 = 0.25$ as shown in Fig. 5. For a fixed wave frequency f and magnetic field gradient α , one could therefore estimate an optimal density in Case I (e.g. for $f = 2.45$ GHz and $\alpha = 5$, the optimal density is $n = 1.6 \times 10^{15} \text{ m}^{-3}$). Other authors have found that there is an optimal density using different approaches [15, 16] for which the absorption in the resonance zone is optimized.

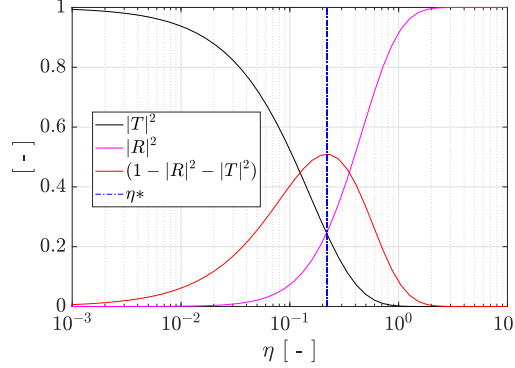


Figure 5. Effect of the dimensionless parameter η on the power ratios of Case I. Transmission and reflection coefficients squared, representatives of the transmitted (black) and reflected (magenta) power with a representative figure of the absorbed power fraction (red).

B. Kinetic effects

While the cold plasma dielectric tensor model successfully describes the wave-plasma interaction away from the resonance, it fails near it, where the phase velocity of the wave becomes comparable to the electron thermal velocity, $\omega/k \sim v_{th} \sim \sqrt{T_e/m_i}$. Assuming a Maxwellian electron species with temperature T_e and a uniform, infinite plasma, the standard kinetic dielectric tensor description results from the integration of the first order perturbation of the electron distribution function f_1 along the zeroth-order trajectories of f_0 with the method of characteristics. This model can be used to obtain the *local* dielectric tensor in the one-dimensional problem of previous section to resolve the resonances [19], although it ignores the effect axial inhomogeneities on its computation.

The contribution of the plasma to the dielectric tensor can be expressed in terms of the *plasma dispersion function* [39] $Z(\zeta)$, defined as

$$Z(\zeta) = \frac{1}{\sqrt{\pi}} \int_{-\infty}^{+\infty} \frac{\exp(-t^2)}{t - \zeta} dt, \quad (21)$$

where the integration path in the complex plane depends on \mathbf{k} and ω as discussed in chapter 9 of Ref. 10. The dispersion relation of the RHP wave propagating parallel to the magnetic field, keeping only electron effects and no collisions, is then given by

$$1 - \frac{k^2 c^2}{\omega^2} + \frac{\omega_{pe}^2}{\omega k v_{th}} Z\left(\frac{\omega - \omega_{ce}}{k v_{th}}\right) = 0. \quad (22)$$

This relation has an infinite number of solutions for k (complex) for each ω (real), a consequence of Z being transcendental. However, only a few of these solutions represent waves of practical interest. This equation may be solved iteratively, starting with the value of k for a cold plasma; this approach however fails for points near the resonance, where the differences are significative with the cold plasma dispersion relation, and a branch continuation algorithm is a more reliable technique. An example of the dominant branch following this approach is shown in Fig. 6, where a large value of v_{th} has been used to exaggerate the kinetic features. As it can be observed, the imaginary part of k remains small except close to resonance, where it reaches large positive values (quick damping).

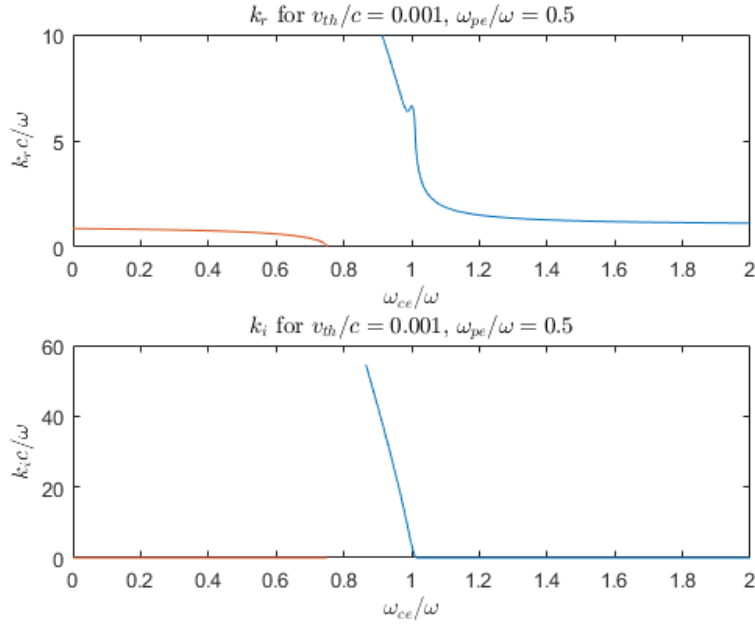


Figure 6. Solution of kinetic dispersion relation for RHP wave and parallel propagation, Eq. (22). A large value of v_{th}/c has been used to exaggerate the kinetic features.

Calling the argument of the Z function $\zeta = (\omega - \omega_{ce})/(kv_{th})$, the series expansion of Z for $|\zeta| \gg 1$ (i.e., far from the resonance) and $|\zeta| \ll 1$ (i.e., near the resonance) is, respectively[10]:

$$|\zeta| \gg 1: \quad Z(\zeta) \sim -\frac{1}{\zeta} \left[1 + \frac{1}{2\zeta^2} \right] + \frac{i}{\sqrt{\pi}} \exp(-\zeta^2), \quad (23)$$

$$|\zeta| \ll 1: \quad Z(\zeta) \sim \frac{i}{\sqrt{\pi}} \exp(-\zeta^2) - 2\zeta \left[1 - \frac{2\zeta^2}{3} \right], \quad (24)$$

where it has been assumed that $\Re(\zeta)\Im(\zeta) < 1$ for the first expression. It is easy to verify that far from the resonance, the cold plasma dispersion relation is recovered in first approximation; the kinetic effects then constitute a small correction only. To first order in $1/\zeta$ but retaining also the exponential term,

$$1 - \frac{k^2 c^2}{\omega^2} \frac{\omega_{pe}^2}{\omega(\omega - \omega_{ce})} - \frac{\omega_{pe}^2 k^2 v_{th}^2}{2\omega(\omega - \omega_{ce})^3} + \frac{i}{\sqrt{\pi}} \frac{\omega_{pe}^2}{\omega k v_{th}} \exp\left(-\frac{(\omega - \omega_{ce})^2}{(k v_{th})^2}\right) = 0. \quad (25)$$

Near the resonance, however, the following approximation is obtained:

$$1 - \frac{k^2 c^2}{\omega^2} - \frac{2\omega_{pe}^2(\omega - \omega_{ce})}{\omega(k v_{th})^2} + \frac{i}{\sqrt{\pi}} \frac{\omega_{pe}^2}{\omega k v_{th}} \exp\left(-\frac{(\omega - \omega_{ce})^2}{(k v_{th})^2}\right) = 0. \quad (26)$$

The imaginary term is responsible for the so-called *cyclotron damping*, a purely kinetic effect that, together with mode conversion[11], explains the absorption of wave power by the plasma at resonance that was discussed in the previous section. It is possible to use this term as a correction of the cold plasma dispersion relation, estimating its value iteratively, so that the resonance can be resolved even in the absence of collisions.

C. Electron susceptibility to the electric field

For a known electric field, e.g. computed with the cold or the kinetic dielectric tensor model, the collisionless electron motion is formally integrable assuming constant parallel velocity of the electrons (i.e., $v_z = \text{const}$), thus neglecting magnetic mirror effect and the axial electric field. The magnetic field is assumed to vary

linearly with distance as in Eq. (13). The equation governing the RHP electron velocity response \hat{v}_- is

$$\frac{d\hat{v}_-}{dt} + i(\omega_{ce} - \omega)\hat{v}_- = -\frac{e}{m_e}\hat{E}_-. \quad (27)$$

Writing v_- as

$$v_-(t) = A(t) \exp(-i\omega t) \exp(-i\omega\alpha v_z t^2/2), \quad (28)$$

the solution is given by

$$\Delta A = -\int \frac{e}{m_e}\hat{E}_-(v_z t) \exp(i\omega\alpha v_z t^2/2) dt. \quad (29)$$

The evolution of the magnitude $|v_-| \equiv |A|$ for a single resonance pass of an example electron is illustrated in Fig. 7(a). Clearly, A is nearly constant away from the resonance, and most of its variation occurs in its neighborhood. Depending on the initial gyrophase, the electrons can gain more or less energy in the resonance pass, and some can even *lose* energy to the field. From Eq. (29), the increment $\Delta A = A_\infty - A_{-\infty}$ across resonance is clearly the same for all electrons with equal parallel velocity v_z , regardless of their initial gyrophase. The group of electrons with same $|A_{-\infty}|$ and v_z lay on a circle of radius $A_{-\infty}$ in the v_x, v_y plane. A single pass through resonance then translates this circle away from the origin by the quantity ΔA as shown in Fig. 7(b). If $|\Delta A| < |A_{-\infty}|$, some electrons lose energy through the resonance. After the resonance pass, the electrons continue to gyrate with $\exp(-i\omega t) \exp(-i\omega\alpha v_z t^2/2)$, and thus this circle rotates about the origin with time.

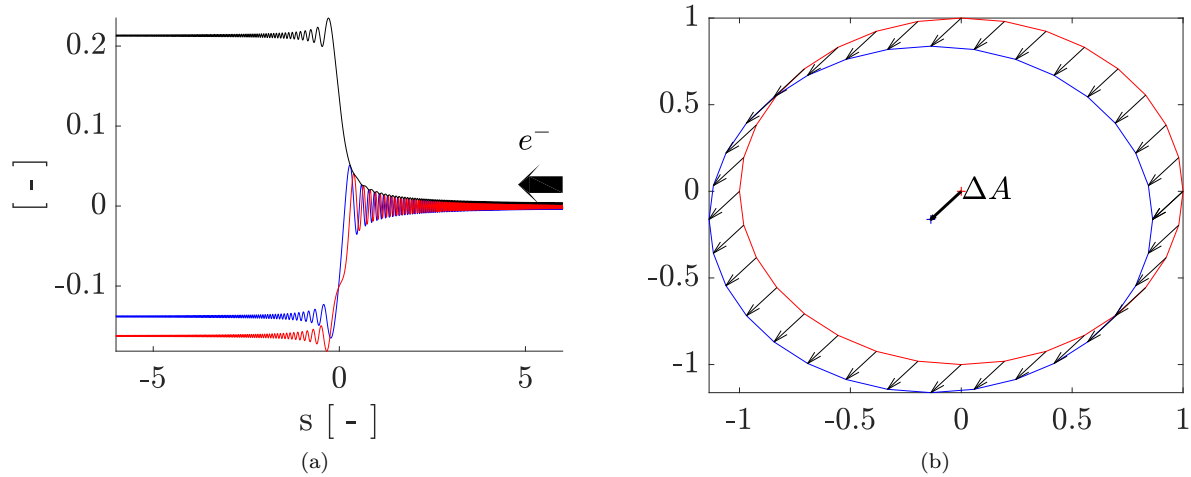


Figure 7. (a) Evolution of the RHP electron velocity v_- as it passes through the resonance. Blue, red and black lines correspond to real, imaginary and the absolute value of δA , respectively. Values are normalized with respect to initial A . (b) Representation of ΔA in the v_x, v_y plane for a group of electrons with identical initial $|v_-|$, whose value has been used to normalize the graph.

The integral of Eq. (29) can be approximated with the stationary phase method, assuming that the electric field oscillates much slower than the phasor:

$$\Delta A \simeq -\int_{-\infty}^{\infty} \frac{e}{m_e}\hat{E}_-(0) \exp(i\omega\alpha v_z t^2/2) dt = -\frac{e\hat{E}_-(0)}{m_e} \sqrt{\frac{\pi}{\omega\alpha v_z}} (1+i). \quad (30)$$

Averaging on the initial gyrophase of the electron and applying the triangle inequality, the increment in electron mechanical energy can be then be estimated as:

$$W_{ecr} \leq \frac{1}{2} m_e \Delta A \cdot \Delta A^* = \frac{\pi e^2 |\hat{E}_-(0)|^2}{\omega\alpha v_z m_e}. \quad (31)$$

This result is also obtained equivalently by [17] and shows that (i) the mean energy gain by electrons due to ECR heating is independent of the phase of the electrons (ii) higher magnetic field gradient, wave frequency, and velocity at the resonant zone decrease the energy gain (iii) the energy gain per pass is sensitive to small changes in electric field at the resonance.

The study of single electron trajectories can be used to compute the kinetic electron response and thus recompute the dielectric tensor $\boldsymbol{\kappa}$, which in turn allows to recalculate the wavefield. Future work will use this approach iteratively to find the self-consistent solution to the 1D wave-plasma problem.

IV. Accuracy of full-wave numerical schemes

Full-wave models provide the wavefield in two or three dimensions, solving simultaneously for all propagating directions in contrast to ray-tracing schemes. While the use of the cold plasma dielectric tensor entails no issues a priori, the kinetic dielectric tensor has the inconvenience of being a function of \mathbf{k} , and is strictly only valid in the limit of a homogeneous, infinite plasma so that the Fourier transform in space is well defined. Use of the kinetic dielectric tensor in full-wave models requires (i) computing the spectrum of \mathbf{k} at each point with a local Fourier transform (or a wavelet transform) and (ii) iteratively computing the kinetic terms[40]. In this section, only the cold plasma model is considered.

Leaving aside spectral methods, the majority of full-wave numerical models can be broadly classified into finite difference, finite volumes, and finite element methods. By large and far, since the advent of computers, the most extended and successful of these techniques for electromagnetic problems have been finite differences[41] (FD) and finite elements[42, 43] (FE):

1. In FD, the differential operators of the wave equations are discretized on a structured grid. These methods are typically simple to analyze and easy to set up and implement. The main drawbacks of FD stem from their reliance on a structured grid: it is difficult to deform the mesh to accommodate complex geometries, or to refine the resolution in a particular region.
2. On the other hand, FE are based on expressing the solution in a vector basis of a given function space. A weak formulation of the problem is used to find the best linear combination of the functions of this basis to represent the solution according to some criterion. The domain is decomposed into cells—elements—of arbitrary size and shape, and the basis functions are selected such that they have a compact support, with non-zero values only in a small number of these elements. FE methods do not rely on a structured grid and thus they can easily deal with complex geometries or regions with different resolutions. As a downside, the formulation and implementation of these methods is more complex than FD, and accuracy assessment is less straightforward.

In all cases, the application of a numerical scheme to the wave equations reduce the problem to a matrix inversion problem $\mathbf{A} \cdot \mathbf{x} = \mathbf{b}$ that can be solved either directly or iteratively. Large problems are usually approached in parallel with multiple processors. For FD, and many FE schemes, the unknowns \mathbf{x} are the values of the electric field components at the nodes of the mesh. A structured, regular Cartesian grid with spacing between nodes given by h_x, h_y, h_z can resolve wavenumbers with real part up to

$$|\Re(k_x)| = \frac{\pi}{2h_x}, \quad |\Re(k_y)| = \frac{\pi}{2h_y}, \quad |\Re(k_z)| = \frac{\pi}{2h_z}. \quad (32)$$

This is known as the Nyquist limit beyond which *aliasing* (i.e., folding of the solution) occurs, and wavenumbers higher than that are mathematically indistinguishable from their corresponding folded wavenumber. We define the *folding box* of a numerical scheme in $\Re(\mathbf{k})$ space with the limits given in Eq. (32).

In this section we discuss the numerical accuracy of FD and FE schemes in 2D and 3D wave-plasma problems in the frequency domain. The accuracy of a given numerical scheme can be analyzed following von Neumann’s technique[44–50]: the discretized equations of the scheme are Fourier-transformed in space assuming an infinite homogeneous plasma and a planar wave traveling in a given direction. The resulting equation can be understood as a *numerical dispersion relation*. This relation can be compared against the analytical dispersion relation, Eq. (6), to find the truncation error. Various types of inaccuracies can arise in the numerical scheme:

1. *Spurious solutions* may exist, not present in the continuous dispersion relation[51, 52].
2. The real part of \mathbf{k} can differ with respect to the continuous dispersion relation. This results in a different wavelength and phase velocity, giving rise to *numerical dispersion*.
3. As a consequence of different dispersion errors in different directions, group velocity errors can exist that affect the direction and rate of transport of power by the wave. We term this *numerical diffusion*.

4. The imaginary part of \mathbf{k} can differ. This results in a different damping rate, giving rise to *numerical dissipation* or *numerical growth*.

Importantly, while the continuous dispersion relation is a function of the angle of propagation with respect to the magnetic field, the numerical dispersion relation depends also on the *angle of propagation with respect to the underlying numerical grid*. While previous studies have analyzed the numerical error of FD and FE schemes, specially for waves propagating in vacuum and in unmagnetized plasmas, and the numerically-induced anisotropy of the grid[53, 54], little effort has been directed toward understanding the interaction of physical anisotropy (due to the magnetic field) and numerical anisotropy, which has already been recognized as a complex problem in the past[55].

To understand the accuracy of the schemes, it is necessary to study how the two matrices in the left hand side of Eq. (6) are approximated. In other words, we must determine the numerical equivalents of k_i^2 , $k_i k_j$, and κ_{ij} , where $i \neq j$ are generic indices. Four FD schemes and one FE schemes have been analyzed in the present work:

1. Second order finite FD with a 3-stencil (**sofd3**). This scheme results directly from the spatial discretization of Eq. (5) using second-order central differences to approximate the second-order derivatives, i.e.,

$$\left. \frac{\partial^2 f}{\partial x^2} \right|^{0,0} \rightarrow \frac{f^{-1,0} - 2f^{0,0} + f^{1,0}}{h_x^2}, \quad (33)$$

$$\left. \frac{\partial^2 f}{\partial x \partial y} \right|^{0,0} \rightarrow \frac{f^{-1,-1} - f^{1,-1} - f^{-1,1} + f^{1,1}}{4h_x h_y}, \quad (34)$$

where the superscripts denote nodal indices with respect to 0, 0, and similarly for other derivatives.

2. Yee's method (**yee**). This scheme is presently the dominant FD one to model wave propagation in vacuum[41]. The first-order derivatives in Eqs. (1) and (2) are discretized with second-order central differences,

$$\left. \frac{\partial f}{\partial x} \right|^{0,0} \rightarrow \frac{-f^{-1,0} + f^{1,0}}{2h_x}. \quad (35)$$

This results in a staggered grid system where the components of $\hat{\mathbf{E}}$ and $\hat{\mathbf{B}}$ are defined at different nodes. The six difference equations can be reduced to three by eliminating $\hat{\mathbf{B}}$ without altering the scheme. Since the components of $\hat{\mathbf{E}}$ are not all defined on each node, interpolation among the neighboring points is required to compute the contribution of the κ matrix to Eq. (6). While this is irrelevant in vacuum where $\kappa_{ij} = 0$ for $i \neq j$, it is central in the case of a plasma. The scheme can be regarded as a 5-stencil scheme.

3. Second order FD method with a 5-stencil (**sofd5**). To obtain this scheme, the second-order derivatives of Eq. (5) are discretized with double grid spacing, whereas the crossed derivatives are discretized with single spacing. In other words,

$$\left. \frac{\partial^2 f}{\partial x^2} \right|^{0,0} \rightarrow \frac{f^{-2,0} - 2f^{0,0} + f^{2,0}}{4h_x^2} \quad (36)$$

and Eq. (34) are used. The obtained scheme has the same approximation for the \mathbf{k} matrix in Eq. (6) as the Yee scheme, but has $\hat{\mathbf{E}}$ defined at each node rather than on staggered grids. Hence, no interpolation in the κ term is required. It can be viewed as a lumped mass matrix Yee method.

4. Fourth order FD method with a 5-stencil (**fofd5**). This scheme results from applying a fourth-order central difference approximation to Eq. (5), i.e.,

$$\left. \frac{\partial^2 f}{\partial x^2} \right|^{0,0} \rightarrow \frac{-f^{-2,0} + 16f^{-1,0} - 30f^{0,0} + 16f^{1,0} - f^{2,0}}{12h_x^2} \quad (37)$$

$$\begin{aligned} \left. \frac{\partial^2 f}{\partial x \partial y} \right|^{0,0} &\rightarrow \frac{1}{144h_x h_y} [(f^{-2,-2} + f^{2,2} - f^{2,-2} - f^{-2,2}) \\ &+ 8(f^{1,-2} + f^{2,-1} + f^{-1,2} + f^{-2,1} - f^{-1,-2} - f^{-2,-1} - f^{1,2} - f^{2,1}) \\ &+ 64(f^{-1,-1} + f^{1,1} - f^{1,-1} - f^{-1,1})] \end{aligned} \quad (38)$$

5. Hexahedral FE method (**hfem**). The Galerkin weak formulation of Eq. (5) results from dot-multiplying it by a test function φ and integrating over the domain[43]. After integrating by parts, this reads:

$$\int \frac{\omega^2}{c^2} \varphi \cdot \kappa \cdot \hat{\mathbf{E}} - \nabla \varphi : \nabla \hat{\mathbf{E}} + (\nabla \cdot \varphi) (\nabla \cdot \hat{\mathbf{E}}) + i\omega\mu_0 \varphi \cdot \hat{\mathbf{j}}_a = 0 \quad (39)$$

Space is discretized into hexahedrals and Q1 functions are used for both the test functions and as the basis to express $\hat{\mathbf{E}}$.

Introducing a planar wave solution $\hat{\mathbf{E}} = \tilde{\mathbf{E}} \exp(i\mathbf{k} \cdot \mathbf{r})$ into the equations of each numerical scheme yields the corresponding numerical dispersion relation. For example, the second order central difference along x of the field \hat{E}_x with Eq. (33) becomes:

$$\frac{\hat{E}_x^{-1,0} - 2\hat{E}_x^{0,0} + \hat{E}_x^{1,0}}{h_x^2} = \frac{\exp(-ik_x h_x) - 2 + \exp(ik_x h_x)}{h_x^2} \tilde{E}_x = -\frac{2 \sin^2(k_x h_x/2)}{h_x} \tilde{E}_x. \quad (40)$$

Table 3 summarizes the effect of these finite approximations to the continuous wave problem. As it can be observed, the effect of the discretizations is the appearance of various sine and cosine factors multiplying the terms in Eq. (6).

The numerical dispersion relation for the first scheme (**sofd3**) in a two dimensional grid in x, y is plotted in Fig. 8 for propagation in vacuum and in a collisionless magnetoplasma regime with $\omega_{pe} = 1.5\omega$, $\omega_{ce} = 2\omega$, and negligible ion contribution to κ , relevant to both ECR thrusters and Helicon plasma thrusters. In vacuum, both wave polarizations coincide and the analytical solution is a double circle with $k = \omega/c$. In the selected magnetoplasma case, both the R and the L waves can propagate. The L wave corresponds to the small oval shape at the center of the figures, and disappears at a higher value of ω_{pe} . The R wave propagates only at small angles with respect to the applied magnetic field \mathbf{B}_0 , and disappears at a resonance cone where $k \rightarrow \infty$, beyond which it becomes an evanescent solution. Figures 9 and 10 show the numerical dispersion relation of the **yee** and **sofd5** schemes in the magnetoplasma case with the resonant cone, when \mathbf{B}_0 forms an angle with the numerical grid, and when electron collisions with a background of neutrals are included, respectively. Finally, Fig. 11 compares the physical solutions of all the schemes introduced above for the vacuum case and the collisionless magnetoplasma case with the resonance cone. In all these figures, k_x and k_y have been normalized with ω/c . The following observations can be made:

Scheme	k_i^2	$k_i k_j$ ($i \neq j$)	κ_{ij} ($i \neq j$)
sofd3	$s^2 \left(\frac{k_i h_i}{2} \right)$	$s(k_i h_i) s(k_j h_j)$	1
yee	$s^2(k_i h_i)$	$s(k_i h_i) s(k_j h_j)$	$c(k_i h_i) c(k_j h_j)$
sofd5	$s^2(k_i h_i)$	$s(k_i h_i) s(k_j h_j)$	1
fofd5	$s^2 \left(\frac{k_i h_i}{2} \right) \frac{4 - c^2(k_i h_i/2)}{3}$	$s(k_i h_i) \frac{4 - c(k_i h_i)}{3} s(k_j h_j) \frac{4 - c(k_j h_j)}{3}$	1
hfem	$\frac{3s^2(k_i h_i/2)}{2 + c(k_i h_i)}$	$\frac{3s(k_i h_i)}{2 + c(k_i h_i)} \frac{3s(k_j h_j)}{2 + c(k_j h_j)}$	1

Table 3. Numerical factors affecting the numerical dispersion relation of each scheme. For each row, the table shows the quantities that multiply the values in the header of each column. The shorthand expressions $s(a) = \sin(a)/a$ and $c(a) = \cos(a)$ have been used. For the **hfem scheme, the numerical dispersion relation has been divided by $(2 + c(k_x h_x))(2 + c(k_y h_y))(2 + c(k_z h_z))/27$ to simplify the expression of the numerical factors shown.**

1. In all cases, the continuous dispersion relation is recovered in the limit $h_i \rightarrow 0$, proving the consistency of all schemes. Numerical dispersion, dissipation and group velocity errors decrease as $k_i h_i$ is decreased. The existence of large k solutions forces the selection of a small grid size h_i to maintain a low $k_i h_i$. This is especially important near a principal resonance or close to the angle of a resonance cone, where k actually goes to infinity in the collisionless limit. The presence of physical dissipation (e.g. collisions) limits the maximum value k that exists near resonance; hence, nonzero dissipation enables the numerical simulation of waves propagating in the resonant directions, and a larger collisionality facilitates the simulation of the problem with a coarser grid.

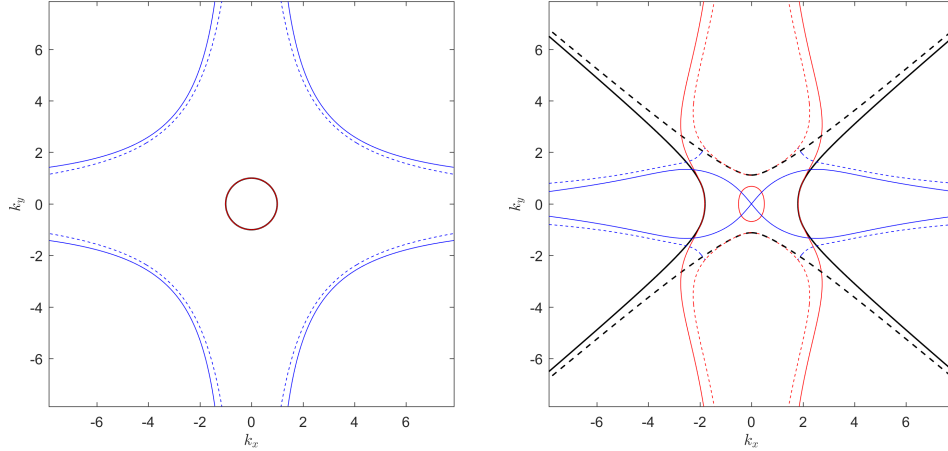


Figure 8. Numerical dispersion relation in vacuum (left) and in the collisionless magnetoplasma regime $\omega_{pe} = 1.5\omega$, $\omega_{ce} = 2\omega$ with B_0 along the x axis (right) for the `sofd3` scheme. The numerical grid spacing has been chosen to be $h_x = h_y = 0.2c/\omega$, and only one folding box is shown. k_x, k_y have been normalized with ω/c . Black lines show the analytic dispersion relation. Red lines show physical numerical solutions. Blue lines show pairs of spurious numerical solutions. Solid and dashed lines denote the real and imaginary parts of k in each direction, respectively.

A small value of h_i is also required to prevent aliasing. The maximum $|\Re(k_i)|$ value that can be successfully simulated, and which defines the folding box as discussed above, is given by Eq. (32).

2. The numerical factors for k_i^2 and $k_i k_j$ ($k_i \neq k_j$) of schemes `yee` and `sodf5` can be simply written as $k_i \rightarrow k_i f(k_i h_i)$, where $f(k_i h_i)$ is a function. In essence, this means that the numerical solution is identical to the analytic solution, except that each k_i suffers some rescaling.

However, the numerical factors for k_i^2 and $k_i k_j$ ($k_i \neq k_j$) of schemes `sofd3`, `fodf5` and `hfem` cannot be written merely as $k_i \rightarrow k_i f(k_i h_i)$, and the effect of the discretization is not just a simple scaling with respect to the analytical \mathbf{k} . This is the cause for the existence of spurious solutions of a first kind in the numerical dispersion relation. These spurious solutions have a $\Re(\mathbf{k})$ comparable to the physical solutions. They appear in pairs: a wave that decays in the direction of propagation, and a wave that grows exponentially, and are thus a dangerous numerical artifact to be avoided. For frequency-domain models, whether spurious solutions manifests depends to a large extent on the boundary conditions of the problem. In time-domain models, spurious solutions are genuinely problematic as they can grow in time. Fig. 8 illustrates the spurious solutions for the `sofd3` scheme.

First-kind spurious solutions are related to a non-zero divergence[51, 52] of the displacement electric field, $\tilde{\mathbf{D}} = \boldsymbol{\kappa} \cdot \tilde{\mathbf{E}}$. Taking the divergence of the homogeneous Eq. (5), it is easy to see that the condition $\nabla \cdot \tilde{\mathbf{D}} = 0$ is equivalent to $\nabla \cdot (\nabla \times \nabla \times \mathbf{E}) \equiv 0$. In \mathbf{k} space, where $\nabla \cdot \rightarrow \mathbf{k} \cdot$, in order to satisfy the divergence-free condition the first matrix in Eq. (6) must vanish when dot-multiplied by \mathbf{k} or its numerical equivalent. Clearly, this does not occur unless we can write $k_i \rightarrow k_i f(k_i h_i)$ for both k_i^2 and $k_i k_j$ ($k_i \neq k_j$) terms.

3. The divergence-free schemes `yee` and `sofd5` can also exhibit pairs of spurious solutions of a second kind in the presence of resonance cones, as shown in Figs. 9 and 10. The cosine factors $\text{inn } \kappa_{ij}$ in the `yee` scheme are responsible of additional warping of the dispersion relation branches at high values of k , with respect to `sofd5`. As a general trend, the latter scheme seems to perform better in this regard for this reason.
4. In all cases there exists *grid-induced anisotropy*, as the effect of the numerical factors differs according to the propagation direction given by \mathbf{k} . This is a well-known effect in vacuum wave propagation[41, 54], and has been illustrated for all schemes in Fig. 11 (left) for a very coarse grid. As a consequence, the numerical dispersion error is different along different propagation directions, and the group velocity,

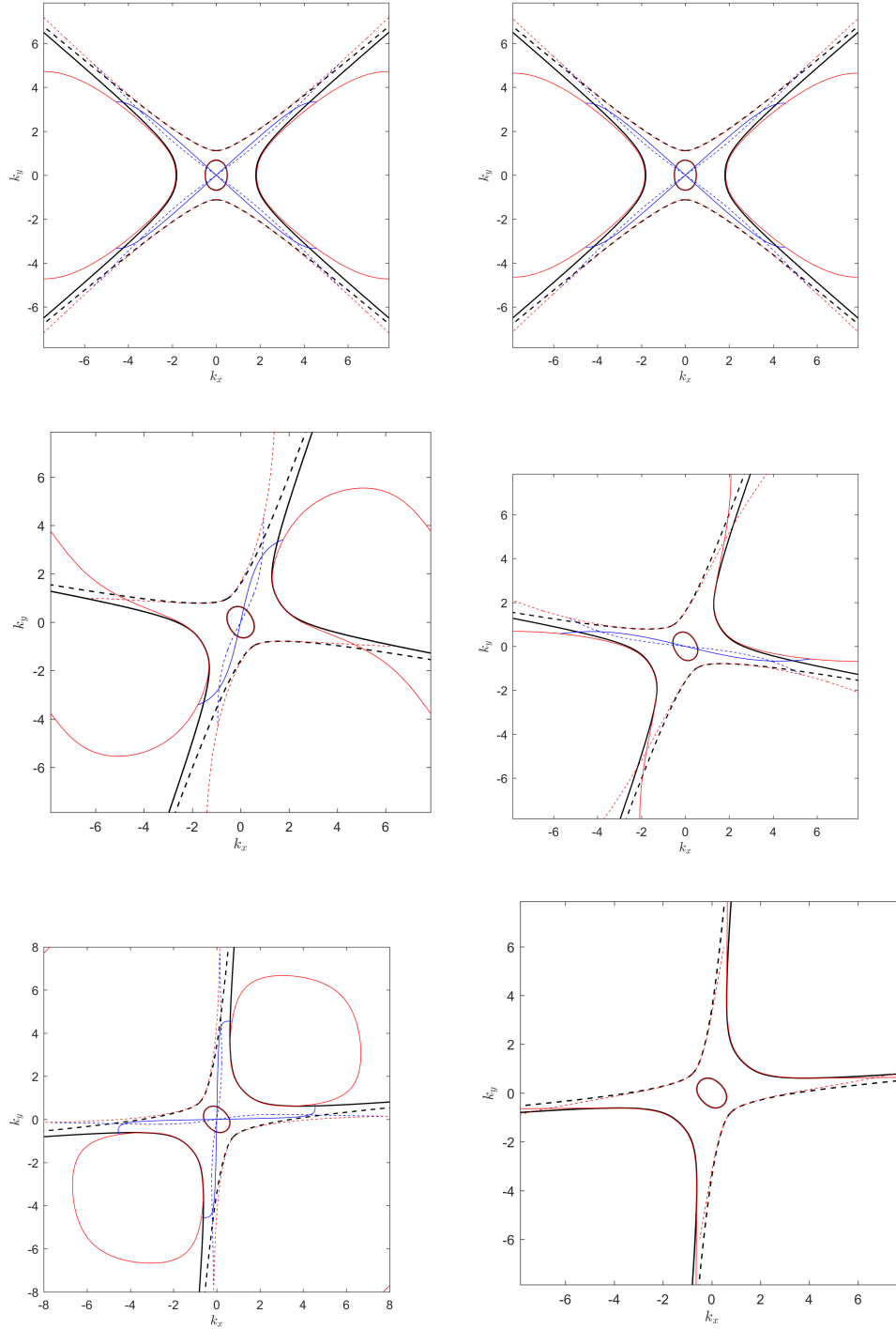


Figure 9. Numerical dispersion relation in the collisionless magnetoplasma regime $\omega_{pe} = 1.5\omega$, $\omega_{ce} = 2\omega$ with B_0 along the x axis (top), forming 30 deg with it (middle) and 45 deg (bottom) for the yee scheme (left) and the sofd5 scheme (right). The numerical grid spacing has been chosen to be $h_x = h_y = 0.2c/\omega$, and only one folding box is shown. k_x, k_y have been normalized with ω/c . Black lines show the analytic dispersion relation. Red lines show physical numerical solutions. Blue lines show pairs of spurious numerical solutions. Solid and dashed lines denote the real and imaginary parts of k in each direction, respectively.

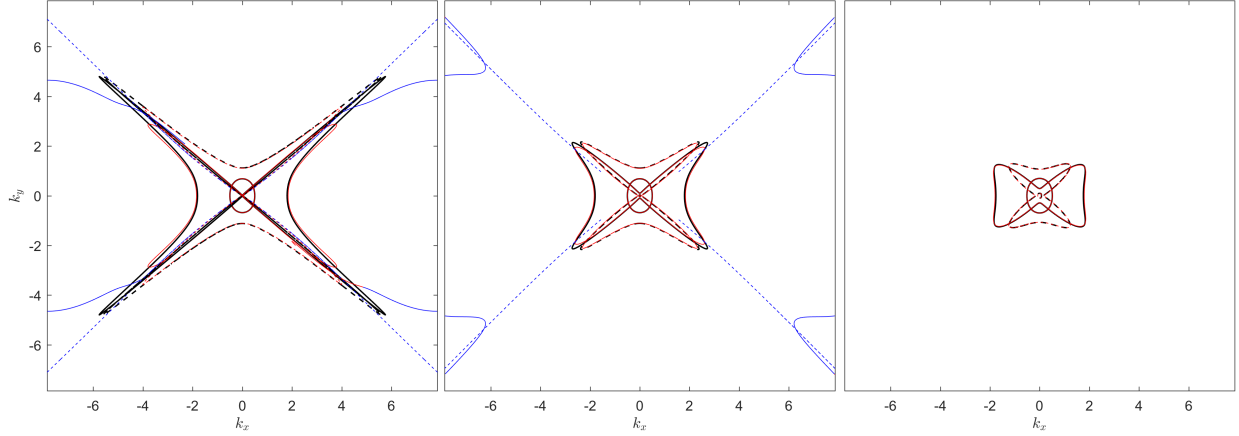


Figure 10. Numerical dispersion relation in the collisional magnetoplasma regime $\omega_{pe} = 1.5\omega$, $\omega_{ce} = 2\omega$ with B_0 along the x axis. The effective electron collisionality is $\nu_e/\omega = 0.002$ (left), 0.01 (middle) and 0.3 (right) for the sofd5 scheme. The numerical grid spacing has been chosen to be $h_x = h_y = 0.2c/\omega$, and only one folding box is shown. k_x, k_y have been normalized with ω/c . Black lines show the analytic dispersion relation. Red lines show physical numerical solutions. Blue lines show pairs of spurious numerical solutions. Solid and dashed lines denote the real and imaginary parts of k in each direction, respectively.

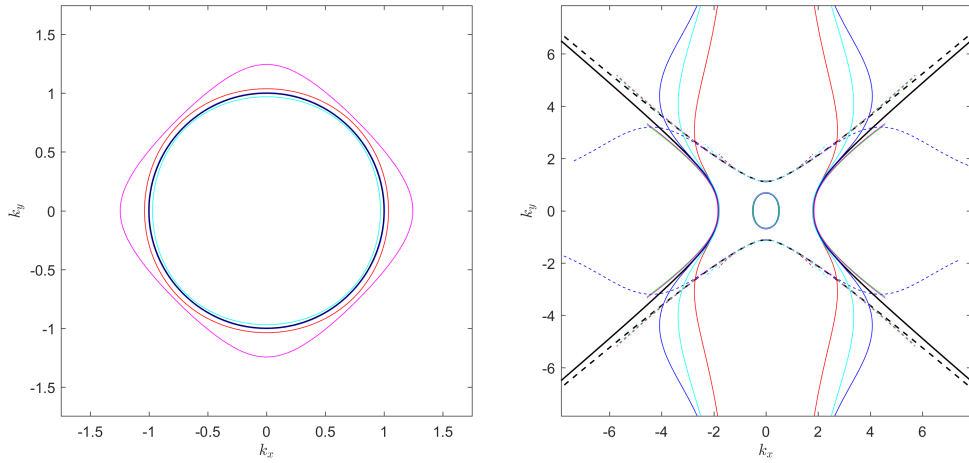


Figure 11. Numerical dispersion relation in vacuum (left) and in the collisionless magnetoplasma regime $\omega_{pe} = 1.5\omega$, $\omega_{ce} = 2\omega$ with B_0 along the x axis (right). The numerical grid spacing has been chosen to be $h_x = h_y = 0.9c/\omega$ in the left figure, and $0.2c/\omega$ in the right figure; only one folding box is shown. k_x, k_y have been normalized with ω/c . Black lines show the analytic dispersion relation. Red, green, blue, magenta and cyan lines correspond to sofd3, sofd5, fofd5, yee and hfem respectively. Only the physical solutions are shown (i.e. no spurious solutions). Solid and dashed lines denote the real and imaginary parts of k in each direction, respectively.

which always points in the direction perpendicular to the dispersion relation curves, also incurs in magnitude and direction errors, i.e. a numerical diffusion error. Different schemes incur in different degrees of numerical anisotropy.

5. This last effect is compounded with the anisotropic nature of the propagation medium in the case of a magnetized plasma. Depending on the relative alignment of the magnetic field with the grid, the error varies. In the case shown in Fig. 11(right), the existence of resonance cones at fixed directions with respect to the magnetic field illustrates the importance of proper grid alignment.

The complexity of the resulting anisotropy problem is evident in Fig. 9, where additional propagating solutions exist in the **yee** scheme for \mathbf{B}_0 forming an angle of 30 and 45 deg from the grid. The spurious solutions (in blue in the figures) disappear for one of the asymptotes of the resonance cone, while they are enhanced near the other. As an exception, the spurious solutions disappear completely in the **sofd5** scheme for \mathbf{B}_0 at 45 deg.

6. Collisionality changes radically the topology of the analytic dispersion relation diagram, capping the maximum value of k in the resonance directions. This is beneficial for numerical simulation, as the collisionless case with $k \rightarrow \infty$ cannot be correctly modeled except with $h \rightarrow 0$.

The spurious solutions the **sofd5** scheme in the collisionless magnetoplasma case of Fig. 9(right) are still present for low collisionality ν_e as shown in Fig. 10. However, the branching point between the physical and spurious solutions now separates into two distinct branches, the spurious one having $\Im(k) < 0$ (i.e., a growing solution). As ν_e/ω is increased, the spurious solution separates further away from the physical ones, and eventually disappears from the folding box. In simulations where these spurious solutions are a problem, this defines a condition between $h_i\omega/c$ and ν_e/ω that must be satisfied to fully avoid the spurious solutions of the second kind.

While beyond the scope of the present work, the effect of axisymmetry, inhomogeneities in the plasma and magnetic field, and a non-uniform numerical grid, on the numerical accuracy are central problems that need to be analyzed in detail. Except for trivial configurations, where a von-Neumann analysis is still viable, the complexity and number of variables in the problem recommend approaching the discussion differently. Inhomogeneities could affect in particular those schemes like **yee** and **hfem** which induce numerical factors in the dielectric tensor $\boldsymbol{\kappa}$ in Eq. (6).

This analysis concludes that divergence-free schemes must be used to avoid spurious solutions of first kind, and that care must be applied to select the right grid step and alignment with respect to the magnetic field, depending on the problem. For these reasons, **yee** and **sofd5** are the chosen options within the category of FD. Between the two, **yee** uses staggered grids and thus less memory for the same accuracy; **sofd5**, in contrast, avoids the interpolation of $\tilde{\mathbf{E}}$ from neighboring nodes, and thus the cosine factors of the **yee** method that affect κ_{ij} . The different subgrids become decoupled only when $\kappa_{ij} = 0$ for $i \neq j$.

In the FE camp, **hfem** is not a good candidate for electromagnetic wave simulation as it is not divergence-free[56]. This obstacle hindered the application of FE method to electromagnetics historically. Other FE schemes, such as the discontinuous edge-element Nedelec approach and the penalty methods where the divergence of \mathbf{D} is included in the weak formulation of the problem[56,57] (not analyzed here), were developed to overcome these limitations. Due to the flexibility of FE methods to define arbitrary meshes, they offer advantages with respect to FD when complex geometries and/or magnetic field topologies are modeled. It has been argued that simplex meshes rather than rectangular grids have the advantage of cancelling part of the numerical error from one element to the next, due to their different relative orientation, thus mitigating the accuracy problem[48]. Experimental FE implementations which include wave features in the basis functions have been proposed for one-dimensional problems[58], but they are hard to extrapolate to higher dimensions[59]. In all cases, modeling problems with low damping requires very fine numerical grids whenever resonance cones are present in the plasma domain.

To conclude, from this analysis the most adequate schemes can be selected to define a 2D axisymmetric code to simulate ECR thrusters. This is the next planned step within the MINOTOR project. Divergence-free FD or FE will be used. The main advantage of FE over FD, i.e. the capability to mesh regions with different levels of refinement, weighs in favor of the latter. The MFEM FE library would be used as the baseline for the code development in that case. A sketch of the intended simulation problem is shown in Fig. 12. The plasma density and magnetic field strength and topology will be provided as inputs from other MINOTOR codes. The angle of the magnetic field with the axis of symmetry varies in the domain. A

perfectly-matched layer (PML) will be implemented on part of the domain boundary to simulate wave losses to free space.

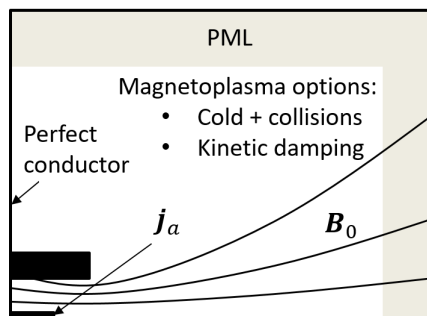


Figure 12. Sketch of the simulation domain for the planned code in the MINOTOR.

V. Conclusions

This paper has reviewed the key physical mechanisms involved in the wave-plasma problem of an ECR thruster, providing references to the main theoretical and experimental works. A one-dimensional parametric study of the right-hand-side wave propagation, cutoff and resonance, and a one-dimensional analysis of the electron motion as a single particle, have been carried out, highlighting the trends that can guide the preliminary design of future thrusters. Future work will use the information of single-electron trajectories to recalculate the dielectric tensor iteratively.

The accuracy of five numerical schemes (four finite differences and one finite element) has been discussed with a von Neumann analysis. The importance of using divergence-free schemes to avoid spurious solutions of the first kind has been stressed. The existence of resonance cones in the analytic dispersion relation is problematic from the numerical treatment: a second kind of spurious solutions can exist, unless sufficient damping is included to limit the maximum analytic value of k . The existence of physical and numerical anisotropy results in a complex dependency of the numerical dispersion relation with the angle formed by the applied magnetic field with the numerical grid.

The wave-plasma simulation strategy of the MINOTOR project has been presented based on this analysis. Finite differences or least-square finite elements with a correct treatment of the divergence of the displacement field (or, alternatively, Nedelec elements) in an axisymmetric geometry will be used to simulate the wave propagation and absorption by the plasma. The MFEM library will be used as the basis for this development. A perfectly-matched layer at the boundary of the simulation domain will account for radiation into free space and avoid power reflection there.

The resulting wave-plasma code is the first module of the SURFET simulation suite to be developed in the MINOTOR project. The development of this suite includes a PIC and a fluid module to simulate the internal dynamics of the plasma using a hybrid approach, and a magnetic nozzle module to model the external plasma expansion and acceleration. All modules are coupled with each other to enable the simulation of a complete ECR thruster; in particular, the wave-plasma module requires the electron density and temperature from the internal fluid code, which in turn receives the information of the power deposition.

Acknowledgments

The research leading to these results has received funding from the European Union H2020 Program under grant agreement number 730028 (Project MINOTOR). Mario Merino's research visit at the Plasma Science and Fusion Center of the Massachusetts Institute of Technology was funded by the Spanish R&D National Plan under grant number ESP2016-75887-P.

References

- ¹Bornatici, M., Cano, R., De Barbieri, O., and Engelmann, F., “Electron cyclotron emission and absorption in fusion plasmas,” *Nuclear Fusion*, Vol. 23, No. 9, 1983, pp. 1153.
- ²Geller, R., *Electron cyclotron resonance ion sources and ECR plasmas*, CRC Press, 1996.
- ³Asmussen, J., Grotjohn, T. A., Mak, P., and Perrin, M. A., “The design and application of electron cyclotron resonance discharges,” *IEEE transactions on plasma science*, Vol. 25, No. 6, 1997, pp. 1196–1221.
- ⁴Miller, D., Bethke, G., and Crimi, G., “Final Report: Investigation of Plasma Accelerator (Cyclotron Resonance Propulsion System),” Tech. rep., NASA Lewis Research Center, November 1, 1965.
- ⁵Miller, D. and Bethke, G., “Cyclotron resonance thruster design techniques,” *AIAA JOURNAL*, Vol. 4, No. 5, 1966.
- ⁶Sercel, J. C., “Electron-cyclotron-resonance (ECR) plasma acceleration,” *AIAA 19th Fluid Dynamics, Plasma Dynamics and Lasers Conference*, 1987.
- ⁷Sercel, J. C., “Electron-Cyclotron-Resonance (ECR) Plasma Thruster Research,” *AIAA 24th Joint Propulsion Conference*, 1988.
- ⁸Sercel, J. C. and Fitzgerald, D. J., “ECR Plasma Thruster Research: Preliminary Theory and Experiments,” *AIAA 25th Joint Propulsion Conference*, 1989.
- ⁹Jarrige, J., Elias, P.-Q., Cannat, F., and Packan, D., “Characterization of a coaxial ECR plasma thruster,” *44th AIAA Plasmadynamics and Lasers Conference, San Diego*, 2013.
- ¹⁰Stix, T. H., *Waves in plasmas*, Springer Science & Business Media, 1992.
- ¹¹Swanson, D. G., *Theory of mode conversion and tunneling in inhomogeneous plasmas*, John Wiley & Sons, 1998.
- ¹²Swanson, D. G., *Plasma waves*, Elsevier, 2003.
- ¹³Lieberman, M. and Lichtenberg, A., *Principles of plasma discharges and materials processing*, Wiley-Blackwell, 2005.
- ¹⁴Musil, J. and Zacek, F., “Penetration of a strong electromagnetic wave in an inhomogeneous plasma generated by ECR using a magnetic beach,” *Plasma Physics*, Vol. 13, No. 6, 1971, pp. 471.
- ¹⁵Brambilla, M., “Self-consistent field and power absorption from electron cyclotron resonance in a high frequency plasma accelerator,” *Plasma Physics*, Vol. 10, No. 4, 1968, pp. 359.
- ¹⁶Kuckes, A., “Resonant absorption of electromagnetic waves in a non-uniformly magnetized plasma,” *Plasma Physics*, Vol. 10, No. 4, 1968, pp. 367.
- ¹⁷Williamson, M. C., Lichtenberg, A. J., and Lieberman, M. A., “Self-consistent electron cyclotron resonance absorption in a plasma with varying parameters,” *Journal of applied physics*, Vol. 72, No. 9, 1992, pp. 3924–3933.
- ¹⁸Koivisto, H., “The effect of microwave frequency and grad B on the energy of electrons in an electron cyclotron resonance ion source,” *Review of scientific instruments*, Vol. 70, No. 7, 1999, pp. 2979–2983.
- ¹⁹Cluggish, B. P. and Kim, J.-S., “Modeling of wave propagation and absorption in electron cyclotron resonance ion source plasmas,” *Nuclear Instruments and Methods in Physics Research Section A: Accelerators, Spectrometers, Detectors and Associated Equipment*, Vol. 664, No. 1, 2012, pp. 84–97.
- ²⁰Stevens, J. E. and Cecchi, J. L., “Wave propagation and plasma uniformity in an electron cyclotron resonance plasma etch reactor,” *Japanese journal of applied physics*, Vol. 32, No. 6S, 1993, pp. 3007.
- ²¹Manheimer, W. M., “A Simple Scheme for Implementing Wave Absorption in Quasi-Neutral PIC Simulations of ECR Plasma,” Tech. rep., Naval Research Lab, Washington DC, Fundamental Plasma Processes, 1998.
- ²²Cardinali, A., Melazzi, D., Manente, M., and Pavarin, D., “Ray-tracing WKB analysis of Whistler waves in non-uniform magnetic fields applied to space thrusters,” *Plasma Sources Science and Technology*, Vol. 23, No. 1, 2014, pp. 015013.
- ²³Muta, H., Sakoda, T., Ueda, Y., and Kawai, Y., “One-dimensional simulation of microwave propagation in electron cyclotron resonance plasmas,” *Japanese journal of applied physics*, Vol. 36, No. 2R, 1997, pp. 872.
- ²⁴Muta, H., Ueda, Y., and Kawai, Y., “Three-dimensional simulation of microwave propagation in an electron cyclotron resonance plasma,” *Japanese journal of applied physics*, Vol. 36, No. 7S, 1997, pp. 4773.
- ²⁵Yasaka, Y., Fukuyama, A., Hatta, A., and Itatani, R., “Two-dimensional modeling of electron cyclotron resonance plasma production,” *Journal of applied physics*, Vol. 72, No. 7, 1992, pp. 2652–2658.
- ²⁶Yasaka, Y. and Uda, N., “Practical scheme for three-dimensional simulation of electron cyclotron resonance plasma reactors,” *Journal of Applied Physics*, Vol. 89, No. 7, 2001, pp. 3594–3601.
- ²⁷Melazzi, D., Curreli, D., Manente, M., Carlsson, J., and Pavarin, D., “SPIREs: A Finite-Difference Frequency-Domain electromagnetic solver for inhomogeneous magnetized plasma cylinders,” *Computer Physics Communications*, Vol. 183, No. 6, 2012, pp. 1182–1191.
- ²⁸Packan, D., Elias, P.-Q., Jarrige, J., Merino, M., Sánchez-Villar, A., Ahedo, E., Peyresoubes, G., Holste, K., Klar, P., Bekemans, M., Scalais, T., Bourguignon, E., Zurbach, S., Mares, M., Hooque, A., and Favier, P., “The MINOTOR H2020 project for ECR thruster development,” *35th International Electric Propulsion Conference*, No. IEPC-2017-547, Electric Rocket Propulsion Society, Fairview Park, OH, 2017.
- ²⁹Batishchev, O., “Minihelicon Plasma Thruster,” *IEEE Transaction on Plasma Science*, Vol. 37, No. 8, 2009, pp. 1563–1571.
- ³⁰Charles, C. and Boswell, R., “Current-free double-layer formation in a high-density helicon discharge,” *Applied Physics Letters*, Vol. 82, No. 9, 2003, pp. 1356.
- ³¹Merino, M., Navarro, J., Ahedo, E., Gómez, V., Sánchez, V., Ruiz, M., Dannenmayer, K., Bosch, E., and González, J., “Maiden tests of the HPT05 helicon plasma thruster prototype,” *Space Propulsion Conference 2016*, No. 3125014, European Space Agency, Rome, Italy, 2016.
- ³²Navarro, J., Wijnen, M., Fajardo, P., Merino, M., Ahedo, E., Ruiz, M., and Gómez, V., “Experimental Performances of a 1-kW HPT by means of Plasma Diagnosis,” *35th International Electric Propulsion Conference*, No. IEPC-2017-447, Electric Rocket Propulsion Society, Fairview Park, OH, 2017.

- ³³Ahedo, E., “Plasmas for space propulsion,” *Plasma Physics and Controlled Fusion*, Vol. 53, No. 12, 2011, pp. 124037.
- ³⁴Merino, M. and Ahedo, E., “Contactless steering of a plasma jet with a 3D magnetic nozzle,” *Plasma Sources Science and Technology*, Vol. 26, No. 9, 2017, pp. 095001.
- ³⁵Brambilla, M., *Kinetic theory of plasma waves: homogeneous plasmas*, Oxford University Press, 1998.
- ³⁶Gaelzer, R., Ziebell, L. F., and Silveira, O. J. G., “Dielectric tensor for inhomogeneous plasmas in inhomogeneous magnetic field,” *Physics of Plasmas*, Vol. 6, No. 12, 1999, pp. 4533–4541.
- ³⁷Budden, K. G., *Radio waves in the ionosphere: the mathematical theory of the reflection of radio waves from stratified ionised layers*, Cambridge University Press, 1961.
- ³⁸Olver, F. W., Lozier, D. W., Boisvert, R. F., and Clark, C. W., *NIST Handbook of Mathematical Functions*, Vol. 5, Cambridge Press, 2010.
- ³⁹Fried, B. D. and Conte, S. D., *The plasma dispersion function: the Hilbert transform of the Gaussian*, Academic Press, 2013.
- ⁴⁰Green, D. L. and Berry, L. A., “Iterative addition of parallel temperature effects to finite-difference simulation of radio-frequency wave propagation in plasmas,” *Computer Physics Communications*, Vol. 185, No. 3, 2014, pp. 736–743.
- ⁴¹Taflove, A. and Hagness, S. C., *Computational electrodynamics*, Artech house, 2005.
- ⁴²Volakis, J. L., Sertel, K., and Usner, B. C., *Frequency domain hybrid finite element methods for electromagnetics*, Morgan & Claypool Publishers, 2006.
- ⁴³Jin, J.-M., *The finite element method in electromagnetics*, John Wiley & Sons, 2014.
- ⁴⁴Marfurt, K. J., “Accuracy of finite-difference and finite-element modeling of the scalar and elastic wave equations,” *Geophysics*, Vol. 49, No. 5, 1984, pp. 533–549.
- ⁴⁵Warren, G. S. and Scott, W., “An investigation of numerical dispersion in the vector finite element method using quadrilateral elements,” *IEEE Transactions on Antennas and Propagation*, Vol. 42, No. 11, 1994, pp. 1502–1508.
- ⁴⁶Cummer, S. A., “An analysis of new and existing FDTD methods for isotropic cold plasma and a method for improving their accuracy,” *IEEE Transactions on Antennas and Propagation*, Vol. 45, No. 3, 1997, pp. 392–400.
- ⁴⁷Lee, J.-F., Lee, R., and Cangellaris, A., “Time-domain finite-element methods,” *IEEE transactions on antennas and propagation*, Vol. 45, No. 3, 1997, pp. 430–442.
- ⁴⁸Wu, J.-Y. and Lee, R., “The advantages of triangular and tetrahedral edge elements for electromagnetic modeling with the finite-element method,” *IEEE Transactions on antennas and propagation*, Vol. 45, No. 9, 1997, pp. 1431–1437.
- ⁴⁹Banks, H., Bokil, V., and Gibson, N., “Analysis of stability and dispersion in a finite element method for Debye and Lorentz dispersive media,” *Numerical Methods for Partial Differential Equations*, Vol. 25, No. 4, 2009, pp. 885–917.
- ⁵⁰Cannon, P. D. and Honary, F., “A GPU-accelerated finite-difference time-domain scheme for electromagnetic wave interaction with plasma,” *IEEE Transactions on Antennas and Propagation*, Vol. 63, No. 7, 2015, pp. 3042–3054.
- ⁵¹Lynch, D. R. and Paulsen, K. D., “Origin of vector parasites in numerical Maxwell solutions,” *IEEE Transactions on Microwave Theory and Techniques*, Vol. 39, No. 3, 1991, pp. 383–394.
- ⁵²Sun, D., Manges, J., Yuan, X., and Cendes, Z., “Spurious modes in finite-element methods,” *IEEE Antennas and Propagation Magazine*, Vol. 37, No. 5, 1995, pp. 12–24.
- ⁵³Young, J., “A full finite difference time domain implementation for radio wave propagation in a plasma,” *Radio science*, Vol. 29, No. 6, 1994, pp. 1513–1522.
- ⁵⁴Bokil, V. A., Gyrya, V., and McGregor, D. A., “A Dispersion Minimized Mimetic Method for Cold Plasma,” *arXiv preprint arXiv:1604.01097*, 2016.
- ⁵⁵Yu, Y. and Simpson, J. J., “An EJ collocated 3-D FDTD model of electromagnetic wave propagation in magnetized cold plasma,” *IEEE Transactions on Antennas and Propagation*, Vol. 58, No. 2, 2010, pp. 469–478.
- ⁵⁶Jiang, B.-n., *The least-squares finite element method: theory and applications in computational fluid dynamics and electromagnetics*, Springer Science & Business Media, 2013.
- ⁵⁷Paulsen, K. D. and Lynch, D. R., “Elimination of vector parasites in finite element Maxwell solutions,” *IEEE Transactions on Microwave Theory and Techniques*, Vol. 39, No. 3, 1991, pp. 395–404.
- ⁵⁸Kohno, H., Bathe, K.-J., and Wright, J. C., “A finite element procedure for multiscale wave equations with application to plasma waves,” *Computers & structures*, Vol. 88, No. 1, 2010, pp. 87–94.
- ⁵⁹Ham, S. and Bathe, K.-J., “A finite element method enriched for wave propagation problems,” *Computers & structures*, Vol. 94, 2012, pp. 1–12.